Article ID: 1000-324X(2022)07-0795-07 **DOI:** 10.15541/jim20210658

High-uniformity Memristor Arrays Based on Two-dimensional $MoTe_2$ for Neuromorphic Computing

HE Huikai[1], YANG Rui[2,3], XIA Jian[3,4], WANG Tingze[3,4], DONG Dequan[3,4], MIAO Xiangshui[2,3]

(1. Nanhu Academy of Electronics and Information Technology, Jiaxing 314002, China; 2. Hubei Yangtze Memory Laboratories, Wuhan 430205, China; 3. Wuhan National Laboratory for Optoelectronics, School of Optical and Electronic Information, Huazhong University of Science and Technology, Wuhan 430074, China; 4. State Key Laboratory of Material Processing and Die & Mould Technology, School of Materials Science and Engineering, Huazhong University of Science and Technology, Wuhan 430074, China)

Abstract: Two-dimensional transition metal dichalcogenides are appealing materials for the preparation of nanoelectronic devices, and the development of memristors for information storage and neuromorphic computing using such materials is of particular interest. However, memristor arrays based on two-dimensional transition metal dichalcogenides are rarely reported due to low yield and high device-to-device variability. Herein, the 2D $MoTe_2$ film was prepared by the chemical vapor deposition method. Then the memristive devices based on 2D $MoTe_2$ film were fabricated through the polymethyl methacrylate transfer method and the lift-off process. The as-prepared $MoTe_2$ devices perform stable bipolar resistive switching, including superior retention characteristics (>500 s), fast switching (~60 ns for SET and ~280 ns for RESET), and excellent endurance (>2000 cycles). More importantly, the $MoTe_2$ devices exhibit high yield (96%), low cycle-to-cycle variability (6.6% for SET and 5.2% for RESET), and low device-to-device variability (19.9% for SET and 15.6% for RESET). In addition, a 3×3 memristor array with 1R scheme is successfully demonstrated based on 2D $MoTe_2$ film. And, high recognition accuracy (91.3%) is realized by simulation in the artificial neural network with the $MoTe_2$ devices working as synapses. It is found that the formation/rupture of metallic filaments is the dominating switching mechanism based on the investigations of the electron transport characteristics of high and low resistance states in the present $MoTe_2$ devices. This work demonstrates that large-scale two-dimensional transition metal dichalcogenides film is of great potential for future applications in neuromorphic computing.

Key words: two-dimensional material; $MoTe_2$; memristor array; neuromorphic computing

The last few years have witnessed rapid progress towards the realization of artificial intelligence (AI), especially software AI thanks to the advances in the development of the algorithm. Note that software AI is typically demonstrated based on the digital computer with conventional Von Neumann architectures at the cost of huge power consumption and massive data throughput[1]. In contrast, hardware AI systems based on in-memory computing architecture can handle probabilistic and unstructured problems with low power dissipation resembling biological neural networks. Recently, memristor has attracted increasing attention as a promising candidate for the construction of hardware neuromorphic computing systems due to its prominent advantages, including simple structure and rich switching dynamics resembling biological synapses and neurons[2-8].

Emerging two-dimensional (2D) materials, especially 2D layered transition metal dichalcogenides (TMDs), are actively studied for fabricating high-performance nanoelectronic devices[9-11]. The 2D TMDs have shown prospective potential for memristor applications, and these devices could be of use in both information storage and neuromorphic computing[12]. Such devices exhibit properties that traditional thin film-based memristors do not have, including high thermal stability[13], high controllability of potentiation, depression and relaxation[14],

Received date: 2021-10-25; **Revised date:** 2021-12-14; **Published online:** 2022-01-06
Foundation item: National Natural Science Foundation of China (U1832116, 51772112)
Biography: HE Huikai (1992–), PhD. E-mail: hehk@hust.edu.cn
何慧凯(1992–), 博士. E-mail: hehk@hust.edu.cn
Corresponding author: YANG Rui, professor. E-mail: yangrui@hust.edu.cn
杨 蕊, 教授. E-mail: yangrui@hust.edu.cn

excellent flexibility and transparency[15]. However, memristors based on 2D TMDs are typically fabricated by mechanical exfoliation, which is not feasible for large-scale array preparation. Thus, the yield and device-to-device variability of 2D TMD-based devices are rarely reported.

Herein, the memristive devices were prepared based on 2D $MoTe_2$ film fabricated by chemical vapor deposition (CVD). This $MoTe_2$ device shows stable bipolar resistive switching with superior retention characteristics, good endurance, high yield, and excellent uniformity. Furthermore, without selector devices, a 3×3 memristor array was demonstrated based on the $MoTe_2$ film. And, a handwritten digits recognition neural network simulation was implemented using the prepared $MoTe_2$ devices as synapses. This work indicates that large-scale 2D TMDs films are promising materials for future neuromorphic computing.

1 Experimental

1.1 Device fabrication

2D $MoTe_2$ film was prepared through the CVD method. Firstly, a 1 nm Mo film was deposited onto a heavily doped Si substrate with 300 nm SiO_2 by electron beam evaporation. Then the Mo film was fully oxidized to MoO_3 in air. The resulting MoO_3 film was placed in a ceramic crucible containing Te powder. A mixture of argon and hydrogen was used as carrier gas and formed a reducing atmosphere during the CVD growth. The MoO_3 film was tellurized into a $MoTe_2$ film after annealing in Te vapor at 700 ℃. The bottom conductive layer (30 nm Au/10 nm Ti) and the top conductive layer (100 nm Au/10 nm Ti) were deposited through DC sputtering and lift-off process. And the $MoTe_2$ film was transferred onto the bottom conductive layer through the polymethyl methacrylate (PMMA) transfer method. The transfer process is shown schematically in Fig. S1.

1.2 Characterization and electrical measurement

The component of the $MoTe_2$ film was measured by Raman spectra with an inVia Reflex spectrometer operated under a 532 nm laser and the XRD measurement (Bruker D8 Advance). An optical microscope (DSX 510) was employed to check the structure of the Au/Ti/$MoTe_2$/Au/Ti device. The thickness and the structure of the memristor array were measured through an atomic force microscope (AFM, SPM9700). All electrical measurements were conducted in air at room temperature with a Keithley 4200 semiconductor characterization system connected with a tabletop cryogenic probe station (PS-100, Lakeshore).

2 Results and discussion

2.1 Composition and structure characterization of the $MoTe_2$ device

Fig. 1(a) shows a typical photo of the $MoTe_2$ film after being transferred on the silicon substrate with bottom electrodes. The film is uniform and continuous across the whole area (~1 cm), as seen from the homogeneous color contrast in the image. And, this thin film is pure $MoTe_2$ without other phases, which is verified by the XRD measurement (Fig. S2). Raman spectroscopy was further employed to investigate the structure of the prepared $MoTe_2$ film, as shown in Fig. 1(b). The $MoTe_2$ film shows several Raman peaks between 100 and 300 cm^{-1}: the out-of-plane A_{1g} mode at ~171 cm^{-1} and the prominent peak of the in-plane E_{2g} mode at ~233 cm^{-1}. These Raman features coincide with those observed in few-layer $MoTe_2$ with the hexagonal (2H) phase, thus unequivocally identifying the as-grown film as 2H $MoTe_2$[16-17].

After characterization of the $MoTe_2$ film, the Au/Ti/$MoTe_2$/Au/Ti device was fabricated through the PMMA transfer method and lift-off process, and the detailed fabrication process is shown in Fig. S3. The optical image of 50 Au/Ti/$MoTe_2$/Au/Ti devices is presented in Fig. 1(c).

In addition to the independent $MoTe_2$ device, a 3×3 memristor array was prepared based on the continuous $MoTe_2$ film. The optical image of the 3×3 memristor array is shown in Fig. 1(d). And the atomic force microscope (AFM) image and height profiles of the prepared array (Fig. S4) demonstrate that the $MoTe_2$ film can

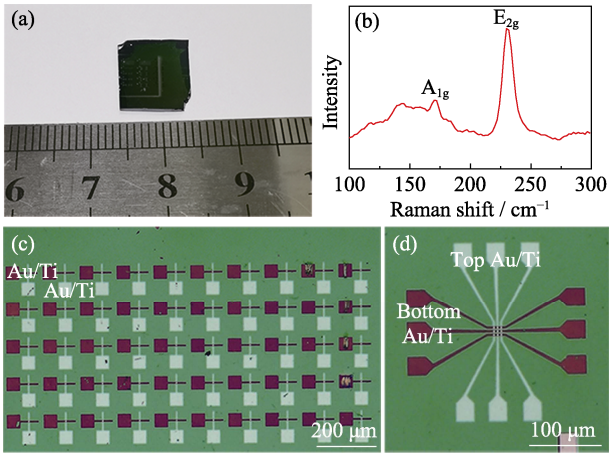

Fig. 1 Characterization of $MoTe_2$ film and electrical measurement of Au/Ti/$MoTe_2$/Au/Ti device

(a) Photo of the centimeter-scale $MoTe_2$ film; (b) Raman spectrum of the $MoTe_2$ film; (c) Optical image of the prepared memristive devices with the structure of Au/Ti/$MoTe_2$/Au/Ti; (d) Optical image of a 3×3 memristor array

adapt to the contour morphology of the bottom electrodes, resulting in a conformal coating.

2.2 Memristive behavior of the Au/Ti/$MoTe_2$/Au/Ti device

After the electroforming process (Fig. S5), stable bipolar resistive switching was obtained when the voltage was swept between –0.8 and 1.0 V, as shown in Fig. 2(a). During a continuous bias sweeping from 0 V→1 V→–0.8 V→0 V, a pinched hysteresis loop was obtained, in which SET (switching from high resistance state (HRS) to low resistance state (LRS)) occurred at about 0.7 V and RESET (switching from LRS to HRS) happened at about –0.5 V. A compliance current of 3 mA was applied in the SET process to prevent hard breakdown. This hysteresis behavior is reproducible in the successive 20 voltage sweeps, indicating the stability of the switching behavior in the present device. The retention characteristics of the $MoTe_2$ device were measured at room temperature, as shown in Fig. 2(b). The ON/OFF ratio is higher than 10 and the current levels of the HRS and LRS show no degradation for 500 s, indicating good retention of the device.

In addition to stable bipolar switching behavior and good retention characteristic, the $MoTe_2$ device exhibits fast switching and good endurance. Current responses of the $MoTe_2$ device under the SET and RESET pulses are presented in Fig. 3(a–b). It was found that the device could be switched to LRS in about 60 ns and switched back to HRS in about 280 ns. Furthermore, over 2000 switching cycles can be obtained under SET pulse of 1.7 V/700 ns and RESET pulse of –1.2 V/7 μs (Fig. 3(c)), indicating good endurance of the present $MoTe_2$ device.

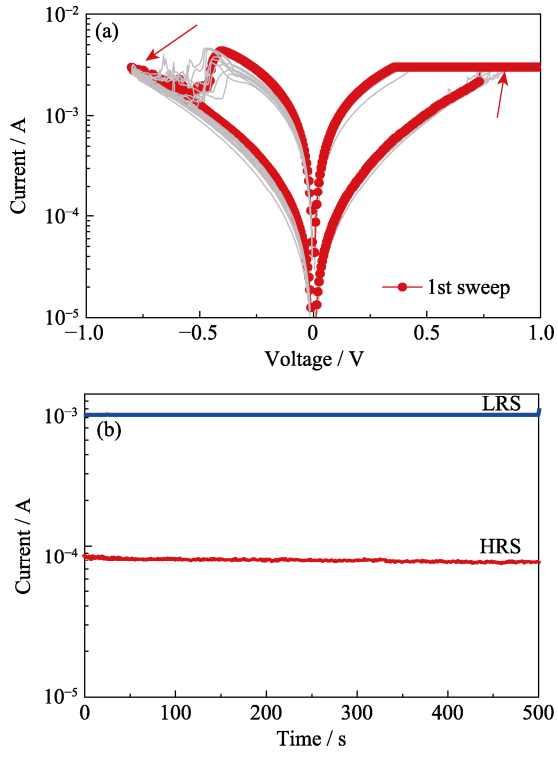

Fig. 2　Stable bipolar resistive switching behavior and retention characteristics of the $MoTe_2$ device

(a) 20 cycles of *I-V* curves with a compliance current of 3 mA; (b) Retention characteristics of the HRS and the LRS read at 0.1 V

2.3 High yield and excellent uniformity of the $MoTe_2$ device

The yield and uniformity of the prepared device are systematically studied, since they are crucial for the construction of large-scale memristor arrays. Among 25 prepared devices, 24 devices show stable bipolar resistive switching behavior similar to that shown in Fig. 2(a), indicating a yield of 96%. We statistically analyzed 480 *I-V* curves collected in 24 devices (detailed results are shown in Fig. S6), and quantified the cycle-to-cycle and the device-to-device variability of the SET voltage (V_{SET}), RESET voltage (V_{RESET}), HRS and LRS by calculating the coefficient of variation (C_V) as the standard deviation (σ) divided by the mean value (μ), in absolute value[18]. The cycle-to-cycle variability in a single device results from the stochastic nature of the switching process, and the device-to-device variability is attributed to inhomogeneity in the samples derived from the fabrication process[19], such as device area and thickness fluctuations, and so on.

The minimum cycle-to-cycle variabilities of V_{SET} and V_{RESET} are 6.6% and 5.2% for a given device, respectively, and the device-to-device variabilities of V_{SET} and V_{RESET} rise to 19.9% and 15.6%, respectively, when considering all 24 devices (Fig. 4). In addition, the device-to-device variabilities of HRS and LRS are 16.8% and 12.7%, respectively (Fig. S7). Note that the device-to-device variabilities of V_{SET} and V_{RESET} are 6.06% and 29.07%, respectively, for the CVD h-BN device reported recently[20], indicating the uniformity of the present device is comparable to that of the h-BN device. Such excellent uniformity makes the $MoTe_2$ film promising for the construction of large-scale memristor arrays.

2.4 Realization of a 3×3 memristor array based on the $MoTe_2$ film

According to the estimation using the one-bit pull-up scheme (detailed results are shown in Fig. S8 and Fig. S9), the maximum array sizes with the 1R scheme and the 1S1R scheme are 4×4 and 870×870 (740 kb), respectively. Therefore, a 3×3 array was fabricated to verify the feasibility of the memristor array based on the $MoTe_2$ film. After an electroforming process, stable resistive switching was achieved in the $MoTe_2$ array device, as shown in Fig. 5(a–b). Notably, due to the inevitable issue of leakage current, the resistance values of the $MoTe_2$ array devices are lower than those of the independent

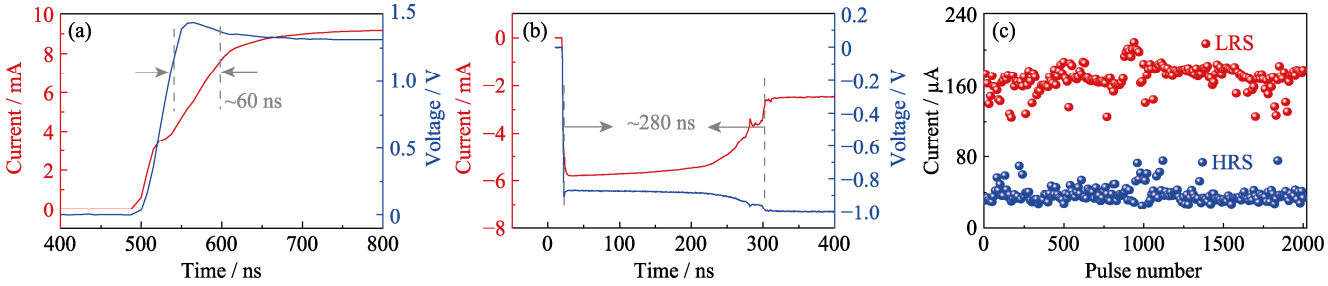

Fig. 3 Fast switching and good endurance of the $MoTe_2$ device

(a) SET speed under the pulse with the amplitude 1.3 V; (b) RESET speed of the $MoTe_2$ device under the pulse with the amplitude of –1.0 V; (c) Over 2000 switching cycles obtained by applying SET pulse of 1.7 V/700 ns and RESET pulse of –1.2 V/7 μs

Colorful figures are available on website

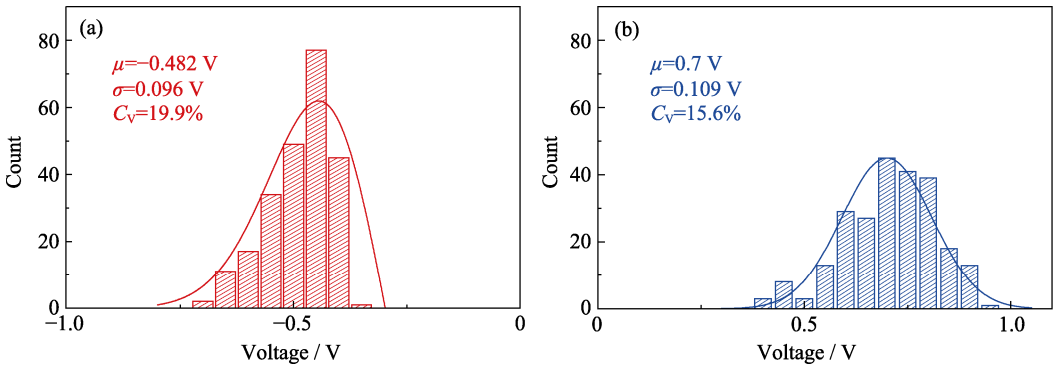

Fig. 4 Cumulative distribution of (a) V_{SET} and (b) V_{RESET} of 24 devices

$MoTe_2$ devices, especially for the HRS, leading to a smaller switching ratio (detailed results are presented in Fig. S10). These results demonstrate that the $MoTe_2$ film is promising for the construction of memristor array, and the array size can be further enlarged through combing with proper selectors.

2.5 Consecutive conductance modulation and neural network simulation of the $MoTe_2$ device

Continuous pulse stimulations are applied on the device to mimic the long-term potentiation (LTP) and depression (LTD) of synapses, which are essential synaptic functions for neuromorphic computing. The conductance triggered by alternating 50 positive (1 V, 500 ns) and 50 negative (–1 V, 5 μs) input pulses exhibits repeatable and stable response of LTP and LTD of biological synapses (Fig. S11).

Fig. 6 presents one cycle of LTP and LTD realized in the present device. The LTP and LTD processes can be fitted by the equation below[21-22]:

$$G = a + c \times e^{-\beta N} \quad (1)$$

where G is conductance, N is the number of pulses, a, c and β are constants. Here, the exponential factor β can reflect the linearity of conductance modulation. The smaller the β, the better the linearities. As shown in Fig. 6, the β for LTP is 0.143 and the β for LTD is 0.203, which is comparable to the previously reported work[21].

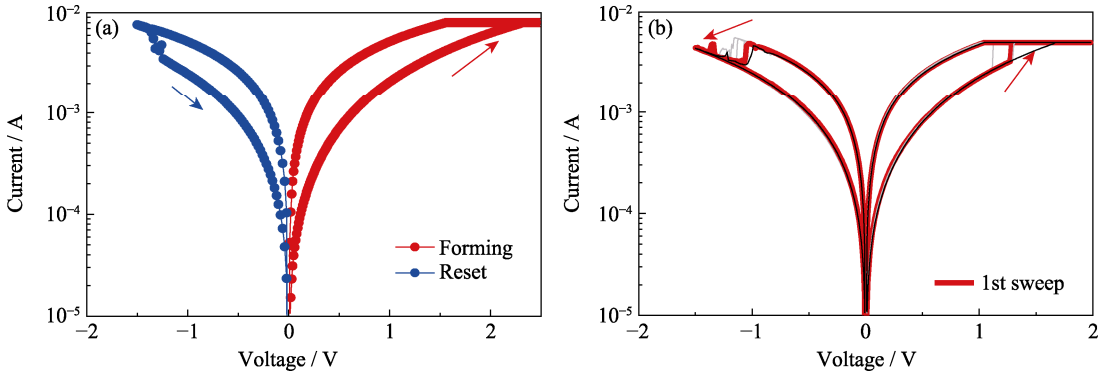

Fig. 5 Stable resistive switching of the $MoTe_2$ array device after electroforming process

(a) Electroforming process of the $MoTe_2$ array device; (b) 20 cycles *I-V* curves of the $MoTe_2$ array device with a compliance current of 5 mA

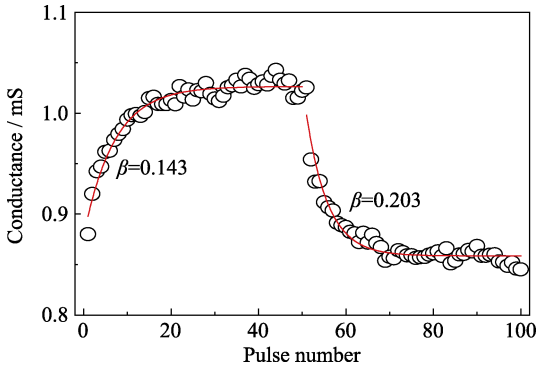

Fig. 6　Potentiation and depression processes of the present device

Circles are experimental results, red lines are fitting results with a phenomenological model $G = a + ce^{-\beta N}$

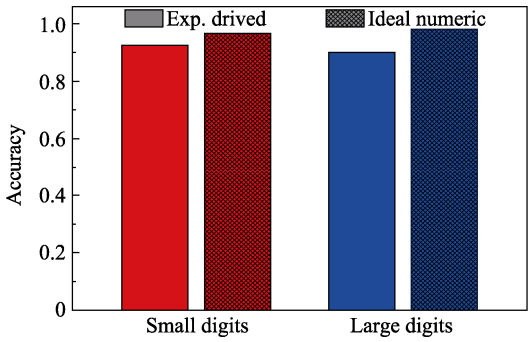

Fig. 7　Recognition accuracy for small and large handwritten digit images with experimental devices and ideal numeric

Colorful figures are available on website

With the present device working as synapses, a fully connected network with one hidden layer has been simulated using the CrossSim platform[23]. The neural network is with 784 input neurons, 300 hidden neurons, and 10 output neurons for 28×28 input pixels and 10 output classifications for recognition handwritten digits from Modified National Institute of Standards and Technology (MNIST) dataset. The $MoTe_2$ devices were used as storage of the weight in the network and the change of the conductance of the artificial synapses was adopted as the weight update in the process of the backpropagation algorithm. In addition, another network with the size of 64×36×10 was trained using another dataset of small digits with 8×8 pixels from the "Optical Recognition of Handwritten Digits" dataset. The test recognition accuracies of the simulation with two datasets using the present device are benchmarked with ideal floating-point numeric precision that represents the neuromorphic algorithm limit, as shown in Fig. 7. The recognition accuracies of the small and large digits can reach ~91.3% and 88.2% after 40 epochs, lower than the ideal numeric accuracies of ~96.7% and 98.1%. This accuracy difference between the experiment derived and the ideal numeric results from the nonlinear and asymmetrical conductance change in LTP and LTD processes, which can be further improved through interface engineering of the device.

2.6　Mechanism analysis

The electron transport processes at LRS and HRS were analyzed to explain the underlying mechanism of resistive switching behavior. As shown in Fig. 8(a), nonlinear *I-V* characteristics are observed at the HRS, with the current increasing as the temperature increases. And it was found that the HRS was best-fitted by the Schottky emission model[24] as shown in the inset of Fig. 8(a);

$$J = A^* T^2 \exp\left[\frac{-q(\varphi_B - \sqrt{qE/4\pi\varepsilon_r\varepsilon_0})}{kT}\right], \quad A^* = \frac{120m^*}{m_0} \tag{2}$$

where A^* is the effective Richardson constant, m_0 is the free electron mass, T is the absolute temperature, q is the electron charge, φ_B is the Schottky barrier height, E is the electric field across the dielectric, k is Boltzmann's constant, ε_0 is the permittivity in vacuum, and ε_r is the optical dielectric constant.

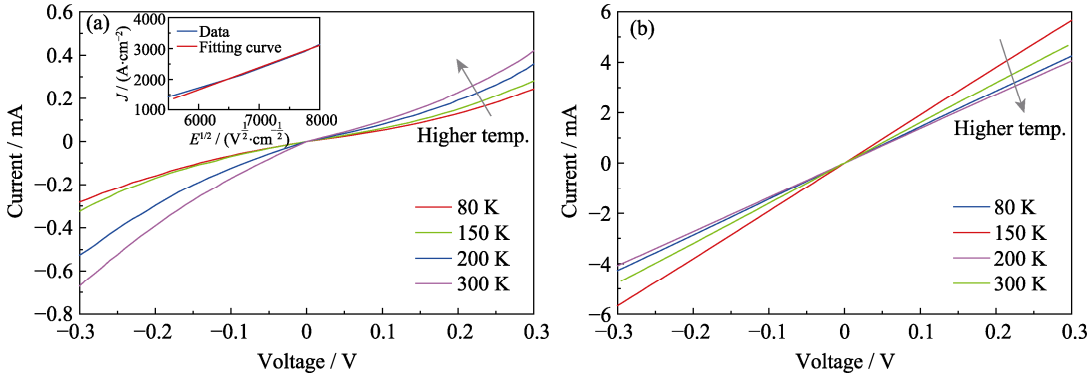

Fig. 8　Mechanism analysis of the memristive behavior in the $MoTe_2$ device

(a) *I-V* characteristics at HRS under different temperatures, with current increasing as the temperature increases. Fitted data using the Schottky emission model for HRS is shown in the inset;

(b) *I-V* characteristics at LRS at different temperatures, with current decreasing as the temperature increase, indicating a metallic characteristic

In contrast, the LRS performs Ohmic conduction due to the linear characteristic of the *I-V* curve (Fig. 8(b)), indicating the formation/rupture of conductive filaments might be the dominating mechanism of the resistive switching. Furthermore, the current of the LRS decreases as the temperature increases, implying the metallic filaments are formed in the LRS. These metallic filaments might be composed of the monoclinic (1T′) phase (1T′-$MoTe_2$) resulting from phase transition of $MoTe_2$[25] or metallic Ti filaments induced by Ti ions drifting into native defects in $MoTe_2$[26]. The detailed atomic structure of these filaments need further investigations.

3 Conclusions

Through CVD growth of the $MoTe_2$ film, the PMMA transfer method and lift-off process, the memristive devices based on 2D $MoTe_2$ film were successfully prepared. The devices exhibit stable bipolar resistive switching with superior retention characteristics and good endurance. More importantly, the devices perform high yield, low cycle-to-cycle variability, and low device-to-device variability. Furthermore, a 3×3 memristor array based on the $MoTe_2$ device with 1R scheme was successfully demonstrated. And, the simulation of neural network with the prepared $MoTe_2$ devices as synapses was implemented for handwritten digits recognition, and the recognition accuracy of around 90% was realized. Our demonstration of memristor array based on centimeter-scale 2D $MoTe_2$ film provides an avenue for future neuromorphic circuits using large-scale 2D TMDs film.

Supporting Materials

Supporting materials related to this article can be found at https://doi.org/10.15541/jim20210658.

References:

[1] SILVER D, SCHRITTWIESER J, SIMONYAN K, *et al*. Mastering the game of Go without human knowledge. *Nature*, 2017, **550(7676):** 354–359.

[2] CHUA L O. Memristor-the missing circuit element. *IEEE Transactions. Circuit Theory*, 1971, **18(5):** 507–519.

[3] STRUKOV D B, SNIDER G S, STEWART D R, *et al*. The missing memristor found. *Nature*, 2009, **459(7250):** 1154.

[4] YANG R, HUANG H M, GUO X. Memristive synapses and neurons for bio-inspired computing. *Advanced Electronic Materials*, 2019, **5(9):** 1900287.

[5] HE H K, YANG R, ZHOU W, *et al.* Photonic potentiation and electric habituation in ultrathin memristive synapses based on monolayer MoS_2. *Small*, 2018, **14(15):** 1800079.

[6] YANG R, HUANG H M, HONG Q H, *et al*. Synaptic suppression triplet-STDP learning rule realized in second-order memristors. *Advanced Functional Materials*, 2018, **28(5):** 1704455.

[7] HE H K, YANG R, HUANG H M, *et al*. Multi-gate memristive synapses realized with the lateral heterostructure of 2D WSe_2 and WO_3. *Nanoscale*, 2019, **12(1):** 380–387.

[8] HUANG H M, YANG R, TAN Z H, *et al*. Quasi-hodgkin-huxley neurons with leaky integrate-and-fire functions physically realized with memristive devices. *Advanced Materials*, 2019, **31(3):** 1803849.

[9] XU M, LIANG T, SHI M, *et al.* Graphene-like two-dimensional materials. *Chemical Review*, 2013, **113(5):** 3766–3798.

[10] FIORI G, BONACCORSO F, IANNACCONE G, *et al*. Electronics based on two-dimensional materials. *Nature Nanotechnology*, 2014, **9(10):** 768–779.

[11] CHANG C, CHEN W, CHEN Y, *et al*. Recent progress on two-dimensional materials. *Acta Physico-Chimica Sinica*, 2021, **37(12):** 2108017.

[12] WANG C Y, WANG C, MENG F, *et al*. 2D layered materials for memristive and neuromorphic applications. *Advanced Electronic Materials*, 2020, **6(2):** 1901107.

[13] WANG M, CAI S, PAN C, *et al*. Robust memristors based on layered two-dimensional materials. *Nature Electronics*, 2018, **1(3):** 203.

[14] SHI Y, LIANG X, YUAN B, *et al*. Electronic synapses made of layered two-dimensional materials. *Nature Electronics*, 2018, **1(8):** 458–465.

[15] HE H K, YANG F F, YANG R. Flexible full two-dimensional memristive synapses of graphene/$WSe_{2x}O_y$/graphene. *Physical Chemistry Chemical Physics*, 2020, **22(36):** 20658.

[16] YAMAMOTO M, WANG S T, NI M, *et al*. Strong enhancement of raman scattering from a bulk-inactive vibrational mode in few-layer $MoTe_2$. *ACS Nano*, 2014, **8(4):** 3895–3903.

[17] GUO H, TENG Y, YAMAMOTO M, *et al.* Double resonance Raman modes in mono- and few-layer $MoTe_2$. *Physical Review B*, 2015, **91(20):** 205415-205415.

[18] ADAM G C, HOSKINS B D, PREZIOSO M, *et al.* 3-D memristor crossbars for analog and neuromorphic computing applications. *IEEE Transactions on Electron Devices*, 2016, **64(99):** 312–318.

[19] SANGWAN V K, LEE H S, BERGERON H, *et al*. Multi-terminal memtransistors from polycrystalline monolayer molybdenum disulfide. *Nature*, 2018, **554(7693):** 500–504.

[20] CHEN S, MAHMOODI M R, SHI Y, *et al*. Wafer-scale integration of two-dimensional materials in high-density memristive crossbar arrays for artificial neural networks. *Nature Electronics*, 2020, **3(10):** 638–645.

[21] WANG Z, YIN M, TENG Z, *et al*. Engineering incremental resistive switching in TaO_x based memristors for brain-inspired computing. *Nanoscale*, 2016, **8(29):** 14015–14022.

[22] BURGT Y, LUBBERMAN E, FULLER E J, *et al.* A non-volatile organic electrochemical device as a low-voltage artificial synapse for neuromorphic computing. *Nature Materials*, 2017, **16(4):** 414–418.

[23] CrossSim platform. https://cross-sim.sandia.gov/ (accessed: July 2019).

[24] ALAMGIR Z, BECKMANN K, HOLT J, *et al*. Pulse width and height modulation for multi-level resistance in bi-layer TaO_x based RRAM. *Applied Physics Letters*, 2017, **111(6):** 063111.

[25] WANG Y, XIAO J, ZHU H, *et al*. Structural phase transition in monolayer $MoTe_2$ driven by electrostatic doping. *Nature*, 2017, **550(7677):** 487.

[26] SHI Y, LIANG X, YUAN B, *et al*. Electronic synapses made of layered two-dimensional materials. *Nature Electronics*, 2018, **1(8):** 458–465.

高均一性二维碲化钼忆阻器阵列及其神经形态计算应用

何慧凯[1], 杨　蕊[2,3], 夏　剑[3,4], 王廷泽[3,4], 董德泉[3,4], 缪向水[2,3]

(1. 中国电子科技南湖研究院, 嘉兴 314002; 2. 湖北江城实验室, 武汉 430205; 3. 华中科技大学 光学与电子信息学院, 武汉光电国家实验室, 武汉 430074; 4. 华中科技大学 材料科学与工程学院, 材料加工与模具技术国家重点实验室, 武汉 430074)

摘　要: 二维过渡金属硫化合物是构建纳米电子器件的理想材料, 基于该材料体系开发用于信息存储和神经形态计算的忆阻器, 受到了学术界的广泛关注。受制于低成品率和低均一性问题, 二维过渡金属硫化合物忆阻器阵列鲜见报道。本研究采用化学气相沉积得到厘米级二维碲化钼薄膜, 并通过湿法转移和剥离工艺制备得到碲化钼忆阻器件。该碲化钼器件表现出优异的保持性(保持时间>500 s)、快速的阻变(SET 时间~60 ns, RESET 时间~280 ns)和较好的循环寿命(阻变 2000 圈后仍可正常工作)。该器件具有高成品率(96%)、低阻变循环间差异性(SET 过程为 6.6%, RESET 过程为 5.2%)和低器件间差异性(SET 过程为 19.9%, RESET 过程为 15.6%)。本工作成功制备出基于 $MoTe_2$ 的 3×3 忆阻器阵列。在此基础上, 将研制的 $MoTe_2$ 器件用于手写体识别, 实现了 91.3%的识别率。最后, 通过对 $MoTe_2$ 器件高低阻态的电子输运机制进行拟合分析, 揭示了该器件阻变源于类金属导电细丝的通断过程。本项工作表明大尺寸二维过渡金属硫化合物在未来神经形态计算中具有巨大的应用潜力。

关　键　词: 二维材料; 碲化钼; 忆阻器阵列; 神经形态计算

中图分类号: TQ125　　**文献标志码:** A

Supporting materials:

High-uniformity Memristor Arrays Based on Two-dimensional $MoTe_2$ for Neuromorphic Computing

HE Huikai[1], YANG Rui[2,3], XIA Jian[3,4], WANG Tingze[3,4], DONG Dequan[3,4], MIAO Xiangshui[2,3]

(1. Nanhu Academy of Electronics and Information Technology, Jiaxing 314002, China; 2. Hubei Yangtze Memory Laboratories, Wuhan 430205, China; 3. Wuhan National Laboratory for Optoelectronics, School of Optical and Electronic Information, Huazhong University of Science and Technology, Wuhan 430074, China; 4. State Key Laboratory of Material Processing and Die & Mould Technology, School of Materials Science and Engineering, Huazhong University of Science and Technology, Wuhan 430074, China)

1 PMMA transfer method

2 XRD analysis of the $MoTe_2$ film

3 Fabrication process of the Au/Ti/$MoTe_2$/Au/Ti device

4 AFM image of the 3×3 memristor array

5 Electroforming process of the device

Before achieving a stable resistive switching, an electroforming process was required, as shown in Fig. S5. At the beginning, the current of the CVD-$MoTe_2$ device was low due to its high resistance. After the application of a relatively large positive voltage (about 1.15 V), the device switched to the LRS.

6 *I-V* curves of 24 Au/Ti/$MoTe_2$/Au/Ti devices

7 Cumulative distribution of device HRS and LRS of 24 devices

8 Estimation of the array size

In case of memristor crossbar array, the cross talk between the adjacent memory cells restricts the maximum possible size of the array. Especially when all memory cells in the array are in low resistance state, the sneak path leakage problem will be highly predominant in the array. Therefore, to obtain the maximum possible crossbar array size, the worst case read scheme is utilized to measure the number of possible word lines with read margin of more than 10%, which is called the one-bit pull-up scheme[1-3].

In this model, the bit line of the selected cell is biased to the read voltage, the word line of the selected cell is grounded and all the other word and bit lines are left floated. Regarding an $N\times N$ square crossbar array with the most challenging data pattern (*i.e.*, all unselected cells in LRS) and negligible line resistance, the crossbar array can be simplified into three regions as shown in the left panel of Fig. S8(a). And the corresponding equivalent circuit is present in the right panel of Fig. S8(a). The resistance value of the selected cell will be found by measuring the output voltage across the pull up resistor, R_{pu}. To obtain the best result during the measurement, the pull up resistor value will be set to the resistance during the low resistance state ($R_{pu}= R_{LRS}$). The read margin normalized to the pull up voltage is calculated by solving the Krichhoff equation:

$$\frac{V_{out}}{R_{pu}}=\frac{R_{pu}}{R_{LRS}^{select}\left\|\frac{2R_{LRS}^{sneak}}{N-1}+R_{pu}\right.}-\frac{R_{pu}}{R_{HRS}^{select}\left\|\frac{2R_{LRS}^{sneak}}{N-1}+R_{pu}\right.} \quad (S1)$$

In order to suppress the leakage current, the memristor can be connected in series with the selector to form a 1S1R (one selector one resistor) structure. The Pt/TaO_x/TiO_2/TaO_x selector reported before was chosen as the selector in combination with the CVD-$MoTe_2$ device to form 1S1R structure since it has an *I-V* window that matches the CVD-$MoTe_2$ device (Fig. S9)[4]. The key resistance values (R_{LRS}^{select}, R_{HRS}^{select}, R_{LRS}^{sneak}) and the corresponding maximum number of word lines/bit lines (N) with read margin >10% for 1R device and 1S1R schemes are listed in Table 1. Note that V_{read} is 2 V.

Fig. S8(b) shows the calculated read margin for both 1R and 1S1R schemes for different number of word lines. From this figure, it is clearly seen that the read margin reduced drastically for 1R scheme and the number of word lines with at least 10% read margin is found to be only 4. In case of 1S1R scheme, the non-linearity of the device resulted in increased number of word lines to 870 for 10% read margin, making a 740 kb possible crossbar array fabrication with good working possibility. Enhancing the selectivity of the selector can result in further increase of the crossbar array size to get a high density and large size crossbar array.

Table 1 Key resistance values and the corresponding maximum number of word lines/bit lines (N) with read margin >10%

Scheme	R_{LRS}^{select}/Ω	R_{HRS}^{select}/Ω	R_{LRS}^{sneak}/Ω	N
1R	150	1500	150	4
1S1R	350	1700	1.25×10^5	870

9　Memristive behavior of the array devices

10　Consecutive conductance modulation of the device

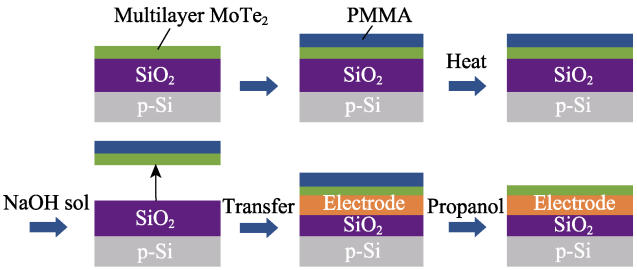

Fig. S1　PMMA transfer method

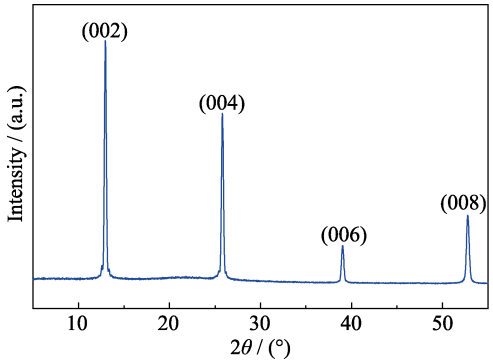

Fig. S2　XRD pattern of the $MoTe_2$ film

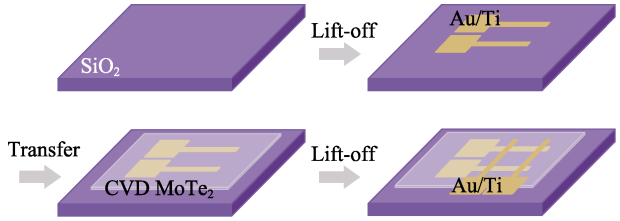

Fig. S3　Fabrication process of the Au/Ti/$MoTe_2$/Au/Ti device

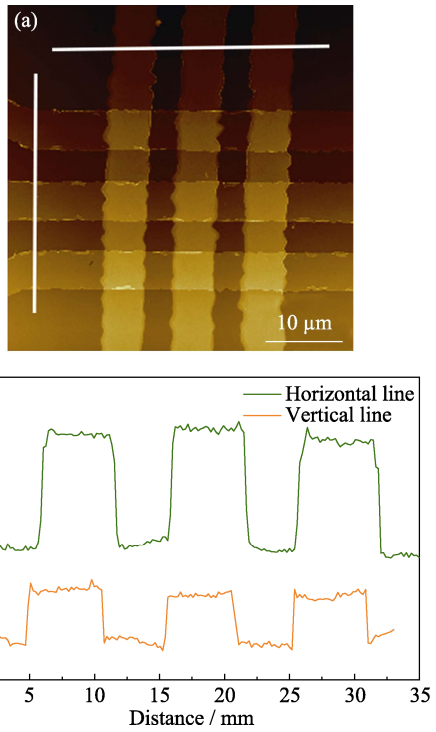

Fig. S4　AFM image (a) of 3×3 memristor array, and the height profile (b) along the horizontal line and the vertical line

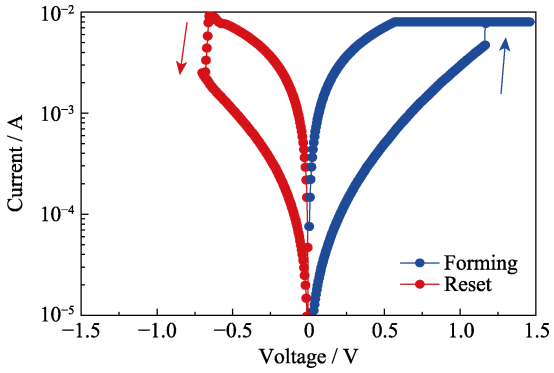

Fig. S5　Electroforming process of the device

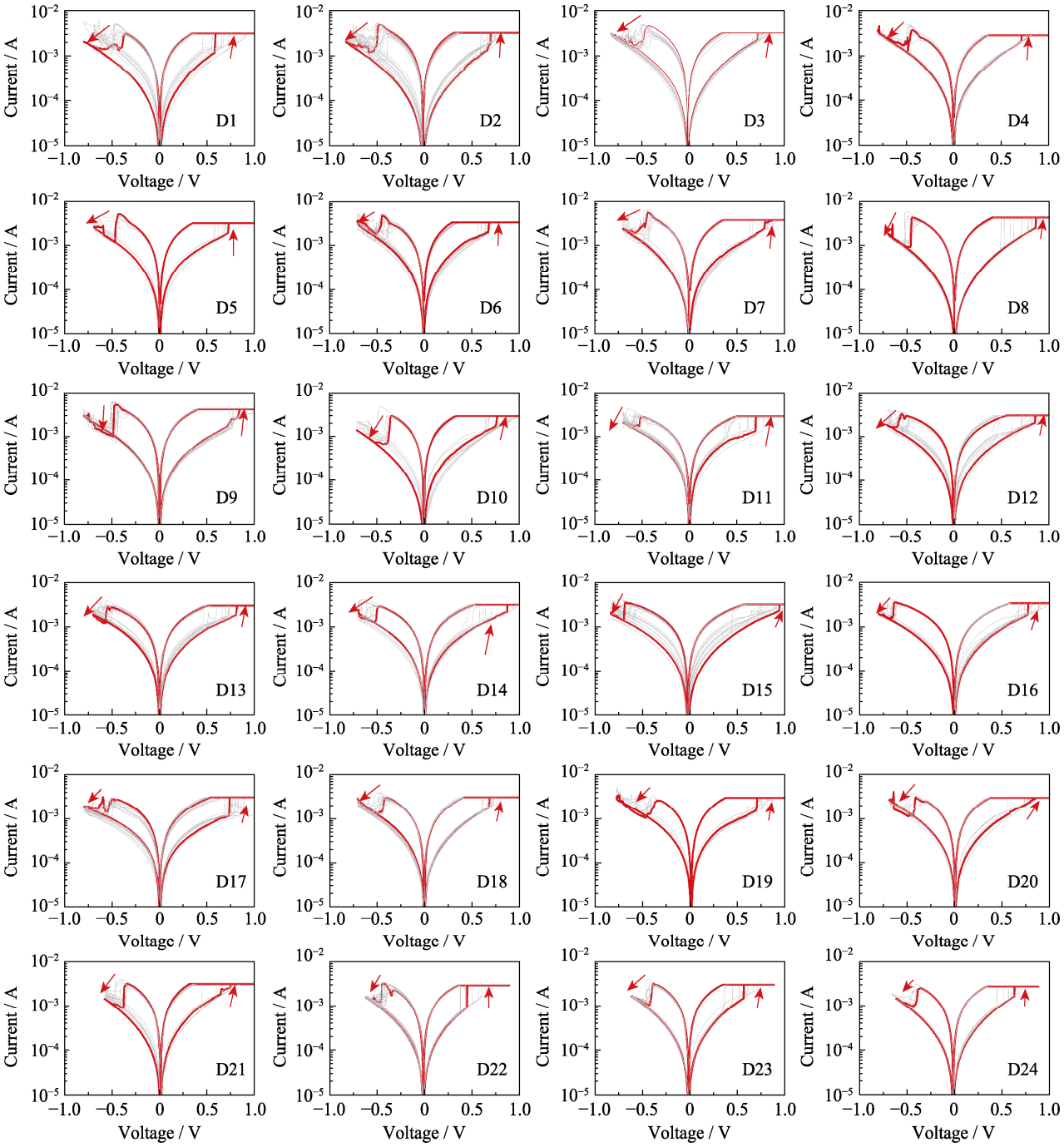

Fig. S6 *I-V* curves of 24 Au/Ti/$MoTe_2$/Au/Ti devices

All devices show stable resistive switching with low cycle-to-cycle and device-to-device variability

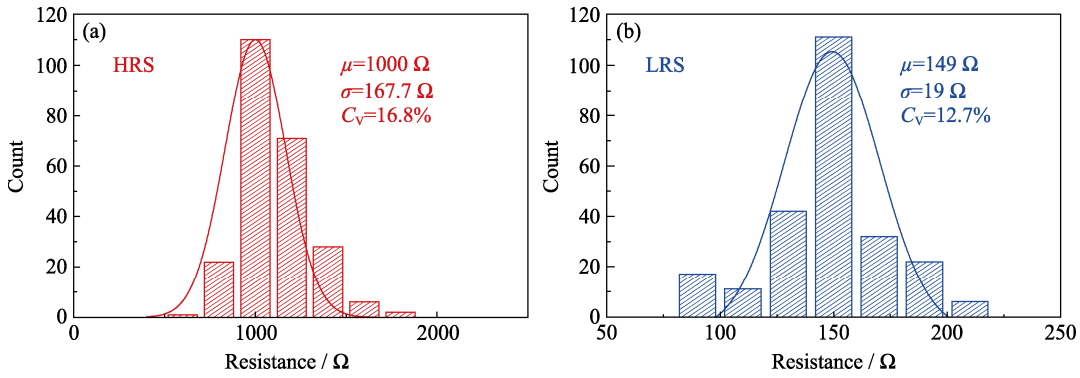

Fig. S7 Cumulative distribution of device (a) HRS and (b) LRS of 24 devices

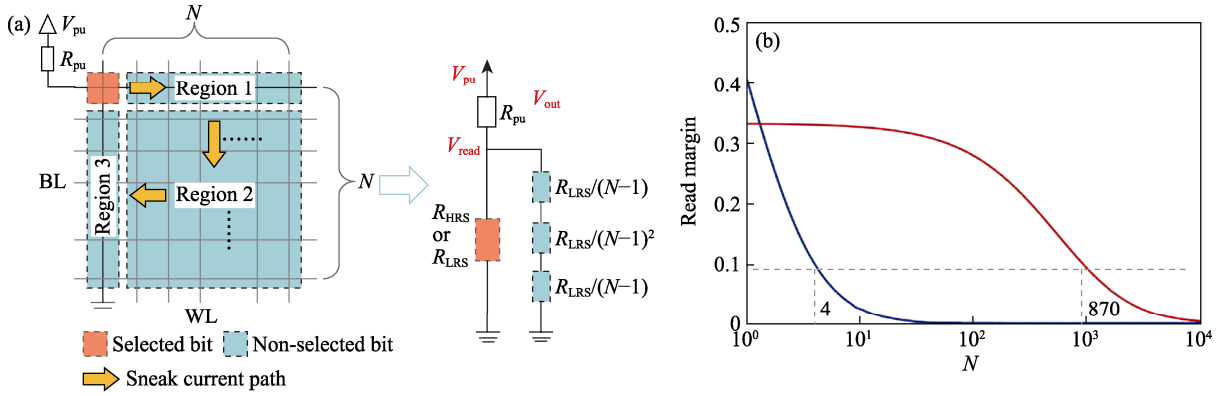

Fig. S8　Estimation of the array size for the prepared CVD-$MoTe_2$ device

(a) Sneak current path at read in a square crossbar array where all bits except the selected one are at LRS, and the equivalent circuit can be represented by three resistors (region 1, region 2 and region 3); (b) Dependence of the read margin on the crossbar line number for both 1R and 1T1R schemes

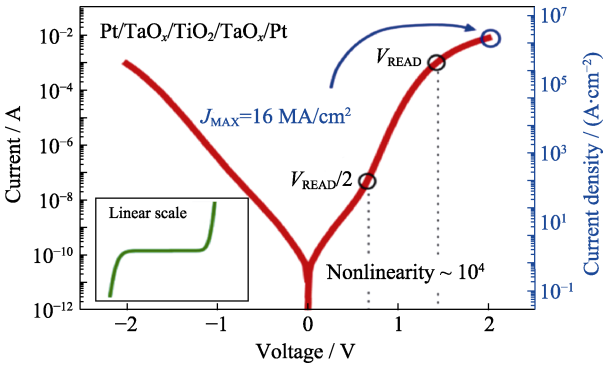

Fig. S9　*I-V* characteristics of the Pt/TaO_x/TiO_2/TaO_x/Pt selector[4]

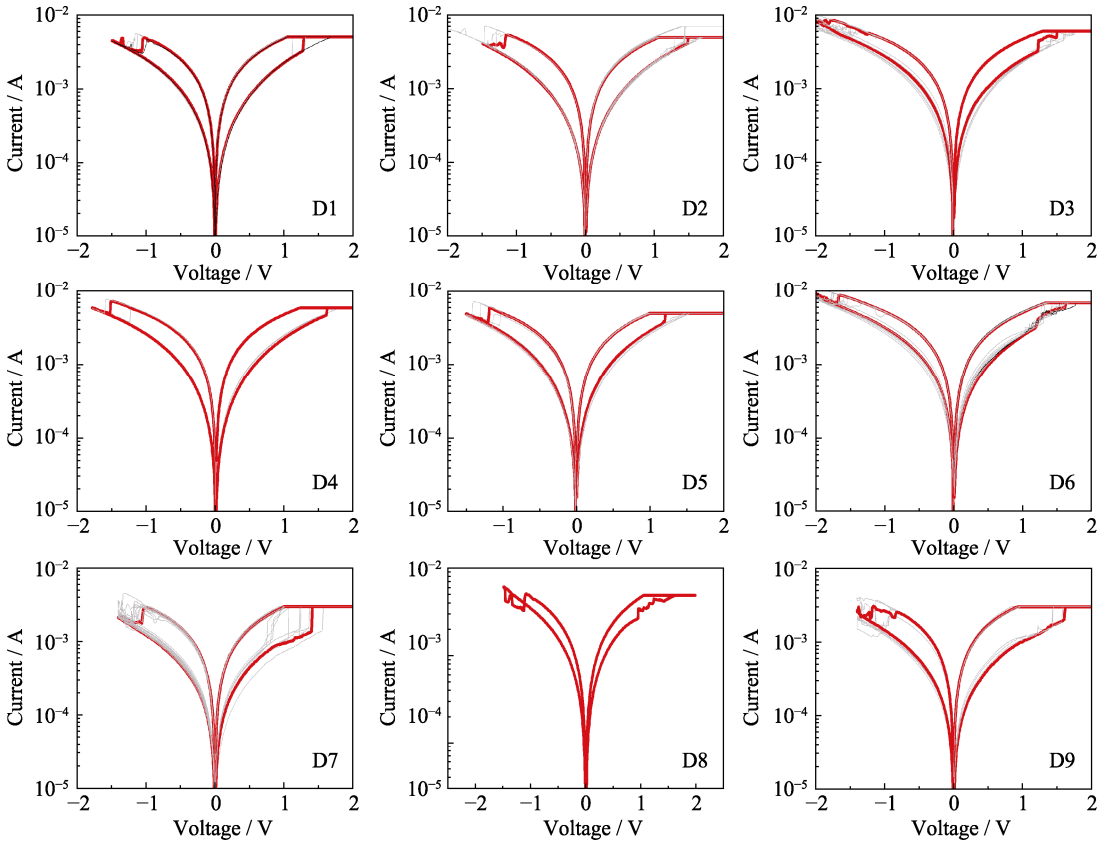

Fig. S10　*I-V* curves of 9 devices in 3×3 array

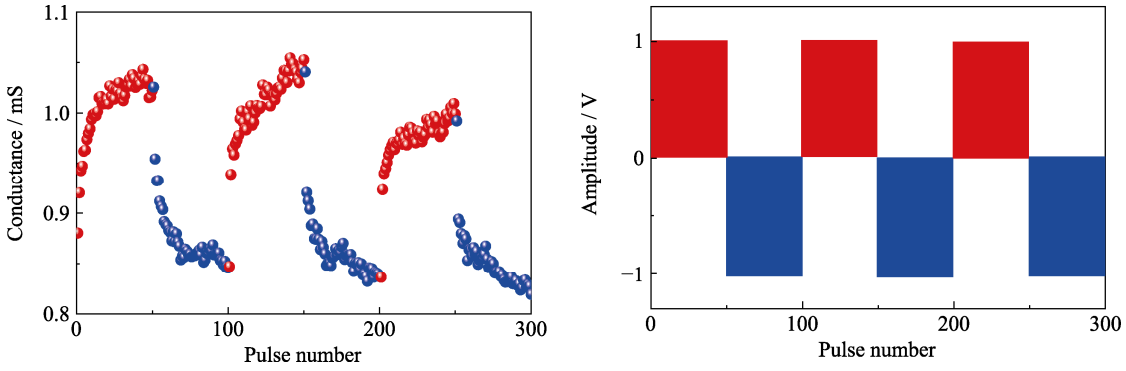

Fig. S11 Long-term potentiation and depression of the device using 50 potentiation (1 V, 500 ns) and depression (–1 V, 5 μs) presynaptic pulses

References:

[1] HUANG J J, TSENG Y M, HSU C W, *et al*. Bipolar nonlinear Ni/TiO_2/Ni selector for 1S1R crossbar array applications. *IEEE Electron Device Letters*, 2011, **32(10):** 1427-1429.

[2] FLOCKE A, NOLL T G. Proceedings of the 33rd European Solid-State Circuits Conference (ESSCIRC, 2007), 2007**:** 328.

[3] LIU Z J. ZnO-based one diode-one resistor device structure for crossbar memory applications. *Applied Physics Letters*, 2012, **100(15):** 041301.

[4] LEE W, PARK J, KIM S, *et al*. High current density and nonlinearity combination of selection device based on TaO_x/TiO_2/TaO_x, structure for one selector-one resistor arrays. *ACS Nano*, 2012, **6(9):** 8166-8172.